

## Vertical design of cubic GaN-based high electron mobility transistors

R. Granzner,<sup>1,a)</sup> E. Tschumak,<sup>2</sup> M. Kittler,<sup>1</sup> K. Tonisch,<sup>1</sup> W. Jatal,<sup>1</sup> J. Pezoldt,<sup>1</sup> D. As,<sup>2</sup> and F. Schwierz,<sup>1,a)</sup>

<sup>1</sup>*Technische Universität Ilmenau, Institut für Mikro- und Nanotechnologien, PF 100565, 98684 Ilmenau, Germany*

<sup>2</sup>*Universität Paderborn, Department Physik, Warburger Str. 100, 33098 Paderborn, Germany*

(Received 28 June 2011; accepted 24 October 2011; published online 1 December 2011)

Cubic (zinc blende) AlGaIn/GaN heterostructures for application in GaN-based high electron mobility transistors are investigated theoretically. The formation of 2DEGs (two-dimensional electron gas) in cubic AlGaIn/GaN structures is studied, carrier distributions and threshold voltages are calculated, and design issues are investigated. For the calculations, a Schrödinger-Poisson solver and a simple analytical model developed in the present work are used. It is shown that due to the barrier doping needed for the formation of a pronounced 2DEG in cubic structures, undesirable saturation effects of the 2DEG density may occur. Options to avoid 2DEG saturation and to realize cubic normally-off HEMTs are elaborated. The behavior of cubic AlGaIn/GaN structures is compared to that of their hexagonal counterparts. © 2011 American Institute of Physics. [doi:10.1063/1.3663364]

### I. INTRODUCTION

Due to the advantageous properties of the AlGaIn/GaN material system, such as large bandgap and high breakdown field, combined with reasonably high electron mobility and high peak velocity, GaN-based HEMTs (high electron mobility transistors) are currently of major interest for high-power, high-temperature, and high-frequency electronics.<sup>1–3</sup> Popular applications for AlGaIn/GaN HEMTs include, among others, microwave power transistors<sup>1,4–6</sup> and power switches.<sup>7,8</sup>

So far, GaN-related research has mainly been focused on hexagonal (wurtzite) AlGaIn/GaN structures.<sup>9–17</sup> Due to strong spontaneous and piezoelectric polarization in hexagonal AlGaIn/GaN heterostructures, a 2DEG (two-dimensional electron gas) channel with very high sheet density is formed at AlGaIn/GaN interfaces.<sup>12,18</sup> Therefore, hexagonal AlGaIn/GaN HEMTs exhibit a significantly enhanced current drive capability compared to, for example, GaAs-based HEMTs.

It has been shown, however, that hexagonal AlGaIn/GaN HEMTs suffer from degradation. Although the reasons or the observed degradation are still under discussion, it seems that the strong polarization in hexagonal AlGaIn/GaN plays a crucial role.<sup>19–22</sup> An alternative to hexagonal AlGaIn/GaN could be cubic (zinc blende) AlGaIn/GaN where polarization effects do not occur. First experimental HEMTs based on cubic GaN have already been demonstrated.<sup>23</sup> Although these first devices lack the exceptional performance of their hexagonal counterparts, theoretical<sup>24–28</sup> and experimental<sup>29,30</sup> studies show similar or even superior material properties of the cubic AlGaIn/GaN system.

The absence of high polarization bound charges at cubic AlGaIn/GaN interfaces has another interesting aspect.

It provides an additional degree of freedom for the design of normally-off transistors.<sup>31</sup> As in GaAs-based HEMTs, doping and thickness of the barrier layer can be adjusted to achieve normally-off operation without affecting the conduction band offset. In hexagonal AlGaIn/GaN HEMTs, on the other hand, the large polarization bound charge can only be reduced by lowering the Al fraction in the barrier. This, in turn, will also lead to a reduction of the conduction band offset at the AlGaIn/GaN interface. The conduction band offset, however, should be as large as possible to prevent the channel electrons from entering the barrier layer and to minimize the detrimental impact of alloy scattering.<sup>32</sup> Moreover, the height of the conduction band offset defines the onset of gate conduction at positive gate biases.<sup>33</sup> This is particularly important for normally-off HEMTs, which need a sufficient gate voltage swing between the positive threshold voltage and the onset of gate conduction.

The aim of this paper is to study design options for cubic GaN-based HEMTs. We focus on the vertical design to clarify the main differences in the electrostatics and the general design rules of cubic AlGaIn/GaN HEMTs compared to their hexagonal counterparts. Special attention is paid to normally-off operation. Our study is based on both numerical self-consistent solutions of the one-dimensional (1 D) Schrödinger and Poisson equations and analytical modeling of the 1 D electrostatics.

The paper is organized as follows. In Sec. II, the details and results of numerical Schrödinger-Poisson solutions are presented. In Sec. III, an analytical model that provides useful insights into the electrostatics of doped cubic AlGaIn/GaN heterostructures is developed and modeling results are compared with those of numerical Schrödinger-Poisson solutions. In Sec. IV, design guidelines for normally-off cubic AlGaIn/GaN HEMTs derived from the analytical model are presented and modeling results for cubic and hexagonal HEMT structures are discussed. Finally, Sec. V concludes the paper.

<sup>a)</sup>Authors to whom correspondence should be addressed. Electronic addresses: ralf.granzner@tu-ilmenau.de and frank.schwierz@tu-ilmenau.de.

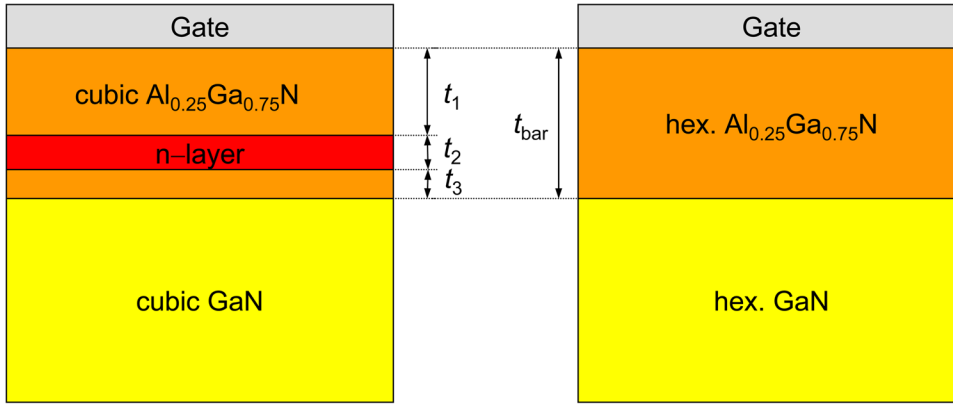


FIG. 1. (Color online) The cubic (left) and hexagonal (right) AlGaIn/GaN heterostructures investigated in this work. The barrier thickness  $t_{\text{bar}}$ , and thus the layer thicknesses  $t_1$ ,  $t_2$ , and  $t_3$  and the doping of the n-layer in the cubic structure have been varied. The hexagonal structure is undoped.

## II. NUMERICAL SCHRÖDINGER-POISSON SOLUTIONS

### A. Studied structures and simulation framework

Figure 1 shows the cubic and hexagonal AlGaIn/GaN heterostructures considered in this work. Due to the absence of polarization effects, the cubic structure has to be doped to form a high-density 2DEG. This is realized by a thin n-doped layer within the AlGaIn barrier separated by intrinsic layers from the electron channel (i.e., the 2DEG) and the gate. All other parts of the cubic structure are undoped. Unintentional background doping is neglected in this study since our intention was to provide general guidelines for the layer design. To this end, the doping level of the n-type layer and the layer thicknesses  $t_1$  (undoped AlGaIn layer underneath the gate),  $t_2$  (n-type AlGaIn layer, doping  $N_D$ ), and  $t_3$  (undoped AlGaIn spacer between n-type layer and GaN channel) have been varied in the simulations. While unintentional doping may slightly modify the results, test simulations have revealed only a minor impact of the background doping for donor concentrations up to  $5 \times 10^{17} \text{ cm}^{-3}$ .

Along the growth direction of AlGaIn/GaN heterostructures, electrons are confined in deep and narrow quantum wells. This requires a self-consistent solution of the 1 D Schrödinger and Poisson equations. We have used our in-house Schrödinger-Poisson solver,<sup>34</sup> which employs the effective-mass approximation and accounts for the nonparabolicity of the central  $\Gamma$  valley.

The material parameters used in this work are summarized in Table I. The effective electron masses  $m_{\parallel}^*$  and  $m_{\perp}^*$  for cubic and hexagonal GaN and AlN are taken from Ref. 35, and the corresponding masses for  $\text{Al}_{0.25}\text{Ga}_{0.75}\text{N}$  are

TABLE I. Material parameters used for the Schrödinger-Poisson simulations of the heterostructures shown in Fig. 1.

	GaN		$\text{Al}_{0.25}\text{Ga}_{0.75}\text{N}$	
	Cubic	Hexagonal	Cubic	Hexagonal
$m_{\parallel}^* (m_0)$ (Ref. 35)	0.193	0.186	0.224	0.220
$m_{\perp}^* (m_0)$ (Ref. 35)	0.193	0.209	0.224	0.239
$E_G$ (eV) (Refs. 18 and 35)	3.070	3.420	3.747	3.910
$\Delta E_C$ (eV) (Ref. 18)			0.427	0.309
Rel. dielectric constant	9.5	9.5	9.5	9.5
Nonparabolicity (Ref. 32)	0.363	0.363	0.332	0.332

obtained by linear interpolation. For the bandgap  $E_G$  we used a nonlinear interpolation model.<sup>18</sup> The relative dielectric constant  $\epsilon_r$  has been assumed to be 9.5 for all materials, which is well within the range of values available in the literature for cubic and hexagonal GaN or AlN. The conduction band offsets  $\Delta E_C$  at the AlGaIn/GaN interfaces were assumed to be 63% of the bandgap differences. Note that, although the band gaps of hexagonal GaN and  $\text{Al}_{0.25}\text{Ga}_{0.75}\text{N}$  are somewhat larger than for the cubic materials, the conduction band offset is smaller in the hexagonal heterostructure.

The spontaneous and piezoelectric polarizations in hexagonal AlGaIn/GaN have been calculated using equations (13) and (43) from Ref. 18, respectively. The discontinuity in the overall polarization at the  $\text{Al}_{0.25}\text{Ga}_{0.75}\text{N}/\text{GaN}$  interface results in a bound polarization charge density of  $1.12 \times 10^{13} \text{ cm}^{-2}$ . It should be noted that in experimental devices partial strain relaxation or the formation of interface states may lead to a reduction of the actual bound charge at the AlGaIn/GaN interface. Such effects, however, strongly depend on the specific fabrication process and are beyond the scope of this work. Our intention is to elaborate the differences in HEMT characteristics and design between cubic and hexagonal material.

### B. Results and discussion

Let us first consider a cubic heterostructure with an overall barrier thickness of 20 nm including a thin 2-nm n-doped  $\Delta$ -layer in the AlGaIn barrier separated by a 3-nm intrinsic spacer from the heterojunction. In Fig. 2 the simulated electron sheet densities are shown as function of the applied surface potential  $E_{CS}$  (i.e., the conduction band edge  $E_C$  at the gate contact) for various donor concentrations  $N_D$ . The upper  $x$  axis shows the gate voltage  $V_G$ , which is related to the surface potential via

$$V_G = -(E_{CS} - \Phi_B)/q, \quad (1)$$

where  $\Phi_B$  is the Schottky barrier height and  $q$  is the elementary charge. We consider a  $\Phi_B$  of 1.4 eV, which is a typical value for Ni/Au contacts on AlGaIn. For each structure, two curves are shown: The overall electron sheet density  $n_S$  and the integrated electron density in the GaN layer only,  $n_{S,\text{GaN}}$ , i.e., the 2DEG sheet density. The difference between these two values corresponds to the integrated electron density in the AlGaIn layer  $n_{S,\text{AlGaIn}}$ . Also shown for comparison are

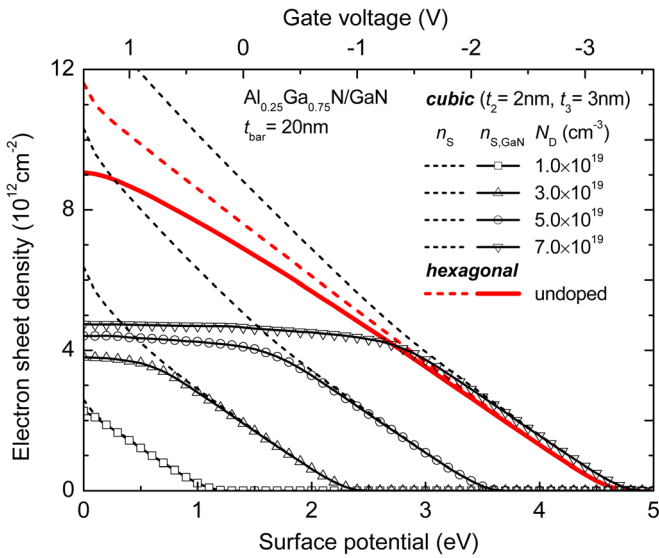


FIG. 2. (Color online) Simulated electron sheet densities as a function of the applied surface potential for cubic heterostructures with various doping levels (complete ionization). For each structure two curves are shown: The overall electron sheet density  $n_S$  (dashed lines) and the integrated electron density in the GaN layer only,  $n_{S,GaN}$  (solid lines). Also shown for comparison are results for an undoped hexagonal heterostructure. The upper  $x$  axis shows the gate voltage assuming a Ni/Au contact with a Schottky barrier of 1.4 eV.

results for an undoped hexagonal heterostructure with the same barrier thickness  $t_{bar}$ .

It is obvious from Fig. 2 that the electron sheet densities in the cubic heterostructure with  $N_D = 1 \times 10^{19} \text{ cm}^{-3}$  are much smaller than in the hexagonal structure. With increasing  $N_D$ ,  $n_S$  can be increased whereas the whole  $n_S(E_{CS})$  curve is shifted along the  $E_{CS}$  axis in positive direction (i.e., the threshold voltage  $V_{th}$  is shifted toward more negative values). For  $N_D > 1 \times 10^{19} \text{ cm}^{-3}$ , however, a saturation of  $n_{S,GaN}$  is observed for surface potentials below a critical value  $E_{CS}^{crit}$ , while the slope of the overall  $n_S(E_{CS})$  curve increases. The reason for this saturation effect is the formation of a second undesirable (parasitic) electron channel in the doped AlGaIn layer as can be seen in Fig. 3. The conduction band edge in the AlGaIn shows a minimum within the

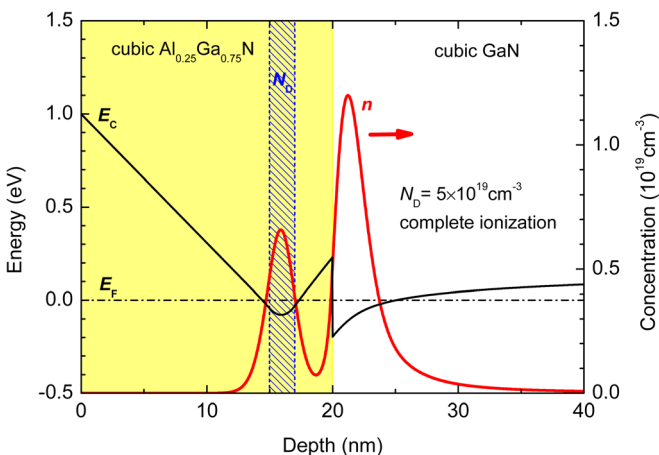


FIG. 3. (Color online) Simulated conduction band edge  $E_C$  and electron distribution in a cubic heterostructure doped with  $N_D = 5 \times 10^{19} \text{ cm}^{-3}$  (complete ionization) biased in the saturation regime.

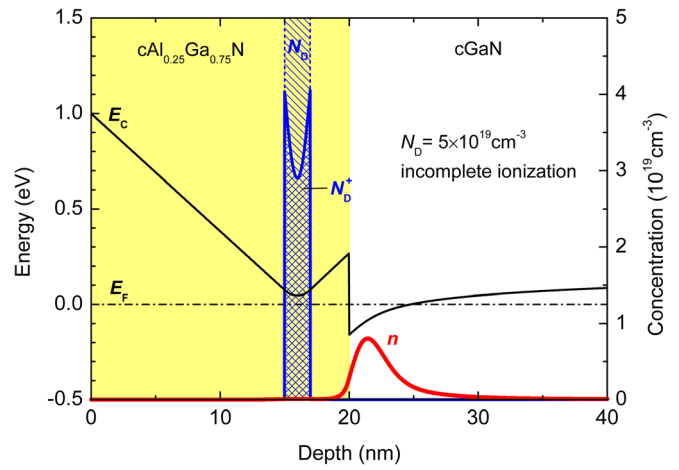


FIG. 4. (Color online) Conduction band edge, electron distribution and density of ionized donors in a cubic heterostructure with  $N_D = 5 \times 10^{19} \text{ cm}^{-3}$  (incomplete ionization). The activation energy of the donors is 20 meV.

doped layer, and for the considered surface potential this minimum is below the Fermi level  $E_F$ . Since in Fig. 3 we considered the donors to be completely ionized, the conduction band in (and close to) the n-type layer is populated by electrons. The negative electron charge in the parasitic channel tends to compensate the positive charge of the ionized donors, which leads to the observed saturation of the 2DEG density  $n_{S,GaN}$ . Since the parasitic channel is located closer to the gate electrode than the 2DEG at the AlGaIn/GaN interface, the gate capacitance, which is inversely proportional to the distance between gate and channel, becomes larger when the parasitic channel is formed. This explains the visible increase of the slope of the overall  $n_S(E_{CS})$  curves in Fig. 2 once  $n_{S,GaN}$  saturates.

If, on the other hand, incomplete ionization of the donors is taken into account, electrons will occupy the donor states before entering the conduction band. This situation is illustrated in Fig. 4, where the density of ionized donors  $N_D^+$  is compared to the total donor concentration. Nevertheless, incomplete ionization also results in a saturation of  $n_{S,GaN}$ , as can be seen in Fig. 5. In this case, however, the critical surface potential is somewhat larger (the corresponding critical gate voltage  $V_{crit}$  is smaller) compared to the case of complete ionization. This is due to the fact that the conduction band edge in the vicinity of the doped layer forms a narrow quantum well for electrons, in which the lowest subband edge is well above the  $E_C$  minimum. To populate this subband by electrons, the  $E_C$  minimum has to be moved below the Fermi level, while in the case of incomplete ionization, those donor states located (in term of energy) slightly below the conduction band edge are occupied. Therefore, in the latter case it is not necessary to move the  $E_C$  minimum below the Fermi level in order to fill the donor states, i.e., compared to complete ionization a smaller gate voltage (larger  $E_{CS}$ ) is required for the onset of saturation.

Which of the two cases is actually closer to reality strongly depends on the doping concentration. As  $N_D$  increases, a semiconductor at low temperatures undergoes an insulator to metal transition, referred to as the Mott transition. In other words, above a critical density all donors can

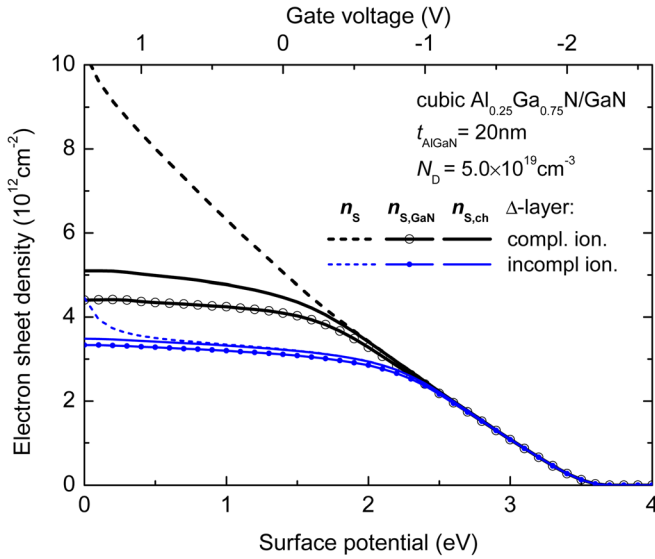


FIG. 5. (Color online) Electron sheet densities as a function of the applied surface potential of a cubic heterostructure with  $N_D = 5 \times 10^{19} \text{ cm}^{-3}$ . The two cases of complete and incomplete ionization are compared.  $n_{s,\text{ch}}$  (solid lines) is the sheet density of channel electrons, which belong to the 2DEG at the heterojunction, including those penetrating into the AlGaIn barrier.

be considered ionized— independent of temperature or Fermi level position. Considering the material parameters of cubic  $\text{Al}_{0.25}\text{Ga}_{0.75}\text{N}$ , Mott transition occurs at a donor concentration of about  $1.4 \times 10^{18} \text{ cm}^{-3}$ .<sup>36</sup> Thus, for the doping levels considered here, the assumption of complete ionization is a good approximation.

In general, a saturation of the 2DEG density at the AlGaIn/GaN interface is undesirable for a HEMT since it leads to a degradation of the transconductance  $g_m$  and hence to a significant deterioration of the frequency performance. The reason is the considerably lower electron mobility in the barrier layer compared to that within the 2DEG, or even worse, due to trapping of electrons in the barrier. Thus, the critical surface potential  $E_{\text{CS}}^{\text{crit}}$ , which corresponds to a critical gate voltage  $V_{\text{crit}}$  basically limits the usable effective gate voltage  $V_{\text{Geff}}$ , where  $V_{\text{Geff}} = V_G - V_{\text{th}}$ . For large signal applications, the difference between  $V_{\text{crit}}$  and  $V_{\text{th}}$  should therefore be as large as possible.

It should be mentioned that the saturation of the 2DEG density is not a problem exclusively related to cubic AlGaIn/GaN heterostructures. It is a well known effect that has first been modeled and discussed for AlGaAs/GaAs HEMTs.<sup>37,38</sup> Based on assumptions similar to those made in Refs. 37 and 38, we can derive analytical expressions for  $V_{\text{crit}}$  and  $V_{\text{th}}$  for the layer structure shown in Fig. 1 (the heterostructures considered in Refs. 37 and 38 are special cases of this layer sequence). Such simple analytical models give useful insights into the device physics and provide general guidelines for the device design.

### III. ANALYTICAL MODELING

Our modeling approach is based on the observation from Figs. 3 and 4 that the conduction band minimum in the AlGaIn barrier is always located within the doped layer (i.e., layer 2 with thickness  $t_2$ ). This is due to the fact that band

bending can only occur in a space charge region. Assuming that the AlGaIn barrier is fully depleted and all donors are ionized, the Poisson equation within layer 2 reads as

$$\frac{d^2\varphi(x)}{dx^2} = -\frac{qN_D}{\epsilon_{\text{bar}}}, \quad (2)$$

where  $\varphi(x) = -E_C(x)/q$  is the potential in the layer 2 (given in volt),  $E_C$  is the conduction band edge,  $x$  is the depth measured from the gate contact, and  $\epsilon_{\text{bar}}$  is the dielectric constant of the barrier. We take the Fermi level as the reference. The solution of Eq. (2) can be easily obtained as the superposition of two contributions,

$$\varphi(x) = \varphi_0(x) + \varphi_{\text{sc}}(x), \quad (3)$$

where  $\varphi_0(x)$  is solution for an undoped heterostructure to which a surface potential  $\varphi_{0\text{S}}$  is applied, and  $\varphi_{\text{sc}}(x)$  is the contribution of the space charge in layer 2 assuming that it induces equal counter charges on both the gate contact and in the 2DEG channel at the AlGaIn/GaN interface. Figure 6 illustrates the shape of both components. From Fig. 6(a) it is clear that  $\varphi_0(x)$  is a linear function of  $x$  given by

$$\varphi_0(x) = -\frac{x}{t_{\text{bar}}^*}(\varphi_{0\text{S}} - \varphi_{\text{ch}}^*) + \varphi_{0\text{S}}, \quad (4)$$

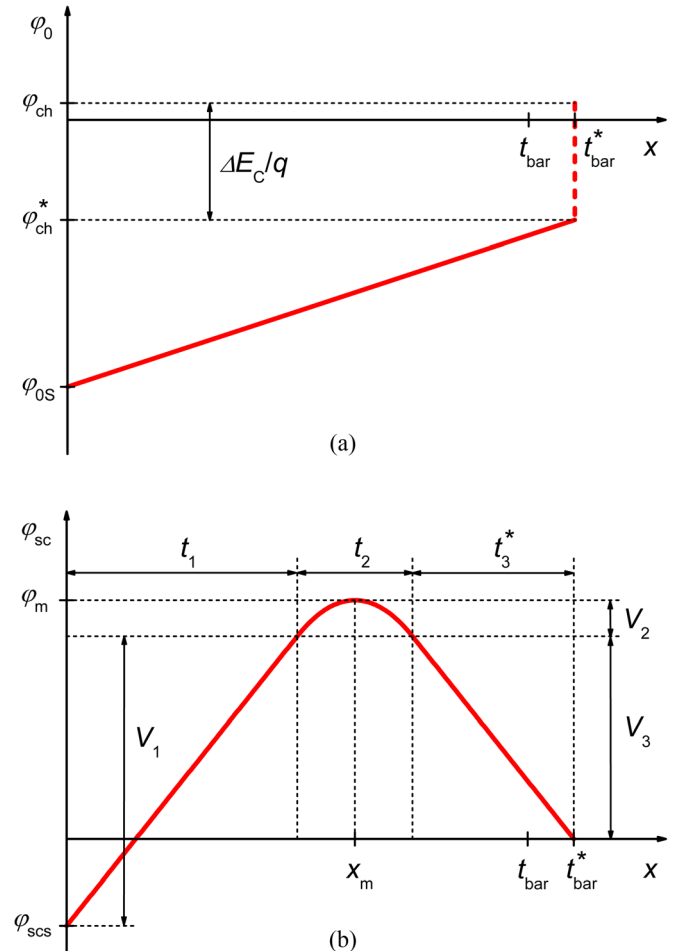


FIG. 6. (Color online) Schematic illustration of the two potential components in Eq. (3): (a)  $\varphi_0(x)$  and (b)  $\varphi_{\text{sc}}(x)$ .

where  $t_{\text{bar}}^*$  is the effective barrier thickness, which accounts for the effective channel thickness  $\delta^*$  as

$$t_{\text{bar}}^* = t_{\text{bar}} + \delta^* (\epsilon_{\text{bar}}/\epsilon_{\text{ch}}), \quad (5)$$

and  $\epsilon_{\text{ch}}$  is the dielectric constant of the channel material. By the effective channel thickness  $\delta^*$ , the effects of two capacitance components in the channel region are modeled: The electrostatic capacitance component related to the average distance  $\delta$  of the 2DEG electrons from the AlGaIn/GaN interface, and the quantum capacitance  $C_q$  which is related to the density of states in the channel.<sup>39,40</sup> Both capacitance components contribute to  $\delta^*$  as

$$\delta^* = \delta + \epsilon_{\text{ch}}/C_q. \quad (6)$$

The potential  $\varphi_{\text{ch}}^*$  in Eq. (4) can be considered as the potential in the barrier at the AlGaIn/GaN interface extrapolated to a position  $(\epsilon_{\text{bar}}/\epsilon_{\text{ch}}) \times \delta^*$  below the interface (see Fig. 6). It is given by

$$\varphi_{\text{ch}}^* = \varphi_{\text{ch}} - \Delta E_C/q, \quad (7)$$

where  $\varphi_{\text{ch}}$  is a fitting parameter<sup>41,42</sup> that is useful when the quantum capacitance is assumed to be constant.

Figure 6(b) illustrates the shape of the second potential component in Eq. (3)—the contribution of the space charge in layer 2,  $\varphi_{\text{sc}}(x)$ . Here we assume that one half of the integrated space charge ( $qN_{\text{D}}t_2/2$ ) induces a counter charge on the gate and the other half induces a counter charge in the 2DEG. For symmetry reasons,  $\varphi_{\text{sc}}(x)$  must have a maximum in the center of layer 2 at  $x_{\text{m}} = t_1 + t_2/2$ , i.e.,  $\varphi_{\text{sc}}(x_{\text{m}}) = \varphi_{\text{m}}$ . The voltage drops across the undoped layers, labeled with  $V_1$  and  $V_3$  in Fig. 6(b), are given by

$$V_1 = Mt_2t_1 \text{ and } V_3 = Mt_2t_3^*, \quad (8)$$

where  $M = qN_{\text{D}}/2\epsilon_{\text{bar}}$  and  $t_3^* = t_3 + \delta^*(\epsilon_{\text{bar}}/\epsilon_{\text{ch}})$ . Solving Poisson's equation in the second half of layer 2, i.e., between  $x = x_{\text{m}}$  and  $x = x_{\text{m}} + t_2/2$ , we arrive at the quadratic equation for  $\varphi_{\text{sc}}(x)$

$$\varphi_{\text{sc}}(x) = -M(x - x_{\text{m}})^2 + \varphi_{\text{m}}, \quad (9)$$

where

$$\varphi_{\text{m}} = V_2 + V_3 = M\left(\frac{t_2}{4} + t_3^*\right)t_2. \quad (10)$$

According to Fig. 6(b), the contribution of the space charge to the surface potential,  $\varphi_{\text{SCS}}$ , is given by

$$\varphi_{\text{SCS}} = V_3 - V_1 = M(t_3^* - t_1)t_2. \quad (11)$$

The surface potential  $\varphi_{\text{S}} = -E_{\text{CS}}/q$  (given in volt) is related to  $\varphi_{0\text{S}}$  and  $\varphi_{\text{SCS}}$  via

$$\varphi_{\text{S}} = \varphi_{0\text{S}} + \varphi_{\text{SCS}}. \quad (12)$$

Due to  $\varphi_{\text{sc}}(x)$  from Eq. (9), Eq. (3) is a quadratic function of  $x$  with a maximum at

$$x_{\text{peak}} = x_{\text{m}} - \frac{1}{2Mt_{\text{bar}}^*} [\varphi_{\text{S}} - M(t_3^* - t_1)t_2 - \varphi_{\text{ch}}^*]. \quad (13)$$

The maximum potential  $\varphi_{\text{max}} = \varphi(x_{\text{peak}})$  corresponds to the conduction band minimum and is a quadratic function of the surface potential  $\varphi_{\text{S}}$ . When  $\varphi_{\text{max}}$  approaches a certain value  $\varphi_{\text{p}}$  close to zero, the electron density in the channel starts to saturate. The corresponding surface potential, which we call the critical surface potential  $\varphi_{\text{crit}} = -E_{\text{CS}}^{\text{crit}}/q$ , is related to the critical gate voltage by  $V_{\text{crit}} = \varphi_{\text{crit}} + \Phi_{\text{B}}/q$ . It is obtained by solving the equation

$$\varphi_{\text{max}}(\varphi_{\text{S}} = \varphi_{\text{crit}}) = \varphi_{\text{p}} \quad (14)$$

leading to

$$\varphi_{\text{crit}} = \frac{qN_{\text{D}}}{C_{\text{G}}} \left( \sqrt{\frac{2\epsilon_{\text{bar}}}{qN_{\text{D}}} (\varphi_{\text{p}} - \varphi_{\text{ch}}^*) + t_3^{*2} - t_3^*} \right) - \frac{qN_{\text{D}}t_2}{\epsilon_{\text{bar}}} x_{\text{m}} + \varphi_{\text{ch}}^*, \quad (15)$$

where  $C_{\text{G}} = \epsilon_{\text{bar}}/t_{\text{bar}}^*$  is the gate capacitance.

Following our approach, the electron sheet charge in the 2DEG consists of two components, namely the contribution of the space charge in layer 2, i.e., the counter charge for one half of the integrated doping density,  $qN_{\text{D}}t_2/2$ , and the charge induced by applying the surface potential  $\varphi_{0\text{S}}$  to an undoped heterostructure given by  $C_{\text{G}} \times (\varphi_{0\text{S}} - \varphi_{\text{ch}}^*)$ . Hence, when a surface potential  $\varphi_{\text{S}}$  smaller than  $\varphi_{\text{crit}}$  is applied, the charge in the 2DEG is given by

$$qn_{\text{S}} = \frac{q}{2}N_{\text{D}}t_2 + C_{\text{G}}[\varphi_{\text{S}} - M(t_3^* - t_1)t_2 - \varphi_{\text{ch}}^*]. \quad (16)$$

At  $\varphi_{\text{S}} = \varphi_{\text{th}}$ ,  $n_{\text{S}}$  vanishes, and from Eq. (16) the threshold surface potential is obtained as

$$\varphi_{\text{th}} = -E_{\text{CS}}^{\text{th}}/q = -\frac{qN_{\text{D}}t_2}{\epsilon_{\text{bar}}}x_{\text{m}} + \varphi_{\text{ch}}^*, \quad (17)$$

which is related to the threshold voltage by  $V_{\text{th}} = \varphi_{\text{th}} + \Phi_{\text{B}}/q$ .

For  $t_1 = 0$ , Eqs. (15) and (17) lead to the expressions derived in Ref. 37. Note that in Ref. 37 an idealized 2DEG was considered, i.e., the effects of the capacitance components of the 2DEG ( $\delta^*$  and  $\varphi_{\text{ch}}$ ) were neglected. Chao *et al.*,<sup>38</sup> on the other hand, considered an ideal planar doping layer in the barrier with zero thickness. Their model can be seen as the extreme case of Eqs. (15) and (17) for  $t_2 \rightarrow 0$  and  $N_{\text{D}} \times t_2 = N_{\text{DS}} > 0$ .

Figure 7 compares the critical and threshold surface potentials calculated from Eqs. (15) and (17), respectively, with those obtained from numerical Schrödinger-Poisson simulations for various  $N_{\text{D}}$ . The surface potentials are given in units of electron volt, i.e., in the form  $E_{\text{CS}}^{\text{crit}}$  and  $E_{\text{CS}}^{\text{th}}$ . The Schrödinger-Poisson results were extracted from simulated  $n_{\text{S, ch}}(E_{\text{CS}})$  curves (see Fig. 5) as follows. First, the  $n_{\text{S, ch}}(E_{\text{CS}})$  curve was approximated by its tangent at the point of maximum slope. Then,  $E_{\text{CS}}^{\text{th}}$  was taken where the tangent crosses the  $x$ -axis at  $n_{\text{S}} = 0$ , whereas  $E_{\text{CS}}^{\text{crit}}$  was taken

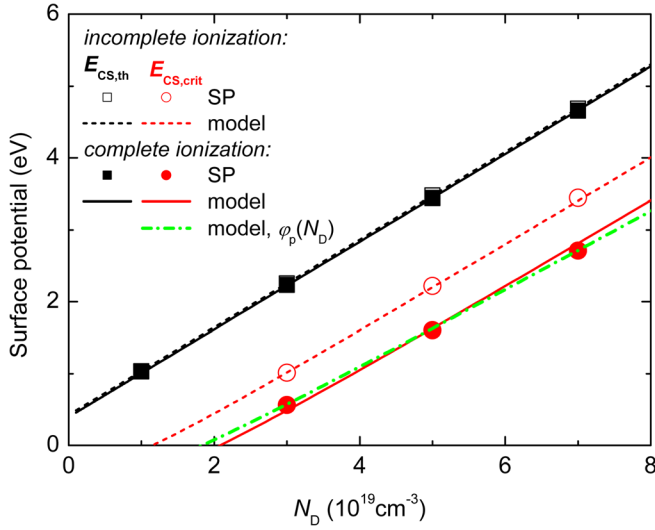


FIG. 7. (Color online) Critical and threshold surface potentials calculated from Eqs. (15) and (17), respectively, compared with those obtained from numerical Schrödinger-Poisson simulations, as a function of  $N_D$ . The fitting parameters ( $\delta^*$ ,  $\varphi_p$ ,  $\varphi_{ch}$ ) for the analytical models are (3.06 nm, -75 mV, 0.97 mV) for incomplete ionization and (2.17 nm, 59 mV, 35 mV) for complete ionization. For the latter case we also considered a linear dependence of  $\varphi_p$  on  $N_D$  (dash-dotted line),  $\varphi_p = a \cdot N_D + b$ , with the fitting parameters  $a = 1.28 \times 10^{-21} \text{ Vcm}^3$  and  $b = 6 \text{ mV}$ .

where the simulated  $n_{s, ch}$  is equal to 95% of the tangent-value.

In Fig. 7, complete and incomplete ionization are considered. For both cases, the agreement between analytical and numerical results is very good. Note that for each case (i.e., for complete and incomplete ionization) a different set of fitting parameters ( $\delta^*$ ,  $\varphi_p$ ,  $\varphi_{ch}$ ) was used. For complete ionization, however, a slight deviation of the analytical  $E_{CS}^{crit}(N_D)$  curve from the numerical results is observed when using a constant  $\varphi_p$ . This is not surprising, since the quantum well for the parasitic channel becomes deeper and narrower when  $N_D$  is increased, and thus the energy separation between the lowest subband and the conduction band minimum increases as well. A perfect agreement between analytical and numerical results is achieved when the doping dependence of  $\varphi_p$  is modeled with a simple linear function,  $\varphi_p = a \cdot N_D + b$ . All fitting parameters are given in the caption of Fig. 7.

#### IV. DESIGN CONSIDERATIONS

Let us now apply our model to the design of a cubic AlGaIn/GaN HEMT. Using Eqs. (15) and (17), we find for the maximum usable effective gate voltage

$$V_{\text{Geff}}^{\text{max}} = \varphi_{\text{crit}} - \varphi_{\text{th}} = \frac{qN_D}{C_G} \left( \sqrt{\frac{2\epsilon_{\text{bar}}}{qN_D} (\varphi_p - \varphi_{\text{ch}}^*) + t_3^{*2}} - t_3^* \right). \quad (18)$$

This gate voltage corresponds to a 2DEG density  $qn_{\text{Smax}} = C_G \cdot V_{\text{Geff}}^{\text{max}}$  that sets a limit for the drain current of a HEMT. Note that  $n_{\text{Smax}}$  is independent of  $C_G$ . Inspecting Eq. (18) reveals that the design parameters defining  $V_{\text{Geff}}^{\text{max}}$  are  $N_D$ ,  $t_3$  and  $t_{\text{bar}}$ . While  $t_{\text{bar}}$  basically defines the slope of the

$n_S(V_G)$  curve, the other two parameters directly affect  $n_{\text{Smax}}$ . Interestingly,  $V_{\text{Geff}}^{\text{max}}$  does not depend on the thickness of the n-type layer  $t_2$ . In other words, a certain doping level of layer 2 has a fixed effect on  $V_{\text{Geff}}^{\text{max}}$ , regardless of the choice of  $t_2$ . This, however, is not yet the full story, since  $t_2$  definitely affects both the critical voltage and the threshold voltage, see Eqs. (15) and (17). For a fixed  $N_D$ , both  $V_{\text{crit}}$  and  $V_{\text{th}}$  become more negative for larger  $t_2$ . The actual effect of  $t_3$  and  $N_D$  on  $V_{\text{Geff}}^{\text{max}}$  becomes clearer, if we rearrange Eq. (18) to

$$V_{\text{Geff}}^{\text{max}} = \frac{2t_{\text{bar}}^* (\varphi_p - \varphi_{\text{ch}}^*)}{\left( \frac{2\epsilon_{\text{bar}}}{qN_D} (\varphi_p - \varphi_{\text{ch}}^*) + t_3^{*2} \right)^{1/2} + t_3^*}. \quad (19)$$

Accordingly, for a large  $V_{\text{Geff}}^{\text{max}}$  a large  $N_D$  is beneficial, whereas  $t_3$  should be as small as possible. The hypothetical upper limit of  $V_{\text{Geff}}^{\text{max}}$  is achieved in the extreme case of infinitely high doping and is given as

$$V_{\text{Geff}}^{\text{max}} = \frac{t_{\text{bar}}^*}{t_3^*} (\varphi_p - \varphi_{\text{ch}}^*). \quad (20)$$

Note that the same expression is found when considering an ideal planar doping layer.<sup>38</sup>

Figure 8 summarizes the effects of the layer structure on  $V_{\text{Geff}}^{\text{max}}$ . It shows  $V_{\text{Geff}}^{\text{max}}$  as a function of the critical surface potential for three combinations of  $t_2$  and  $t_3$ . For each combination, the variation of the critical surface potential is achieved by varying  $N_D$ . The barrier thickness is 20 nm in every case. As can be seen, our analytical model describes the results obtained from Schrödinger-Poisson simulations very well. The largest  $V_{\text{Geff}}^{\text{max}}$  is calculated for the structure with  $t_2 = 2 \text{ nm}$  and  $t_3 = 3 \text{ nm}$ . Increasing either  $t_2$  or  $t_3$  reduces  $V_{\text{Geff}}^{\text{max}}$  for fixed  $E_{\text{CS}}^{\text{crit}}$ . Note that the effect of  $t_2$  is related to the simultaneous shift of both critical and threshold surface potentials, i.e., for the same  $E_{\text{CS}}^{\text{crit}}$  the structure with  $t_2 = 2 \text{ nm}$  can be much higher doped compared to the

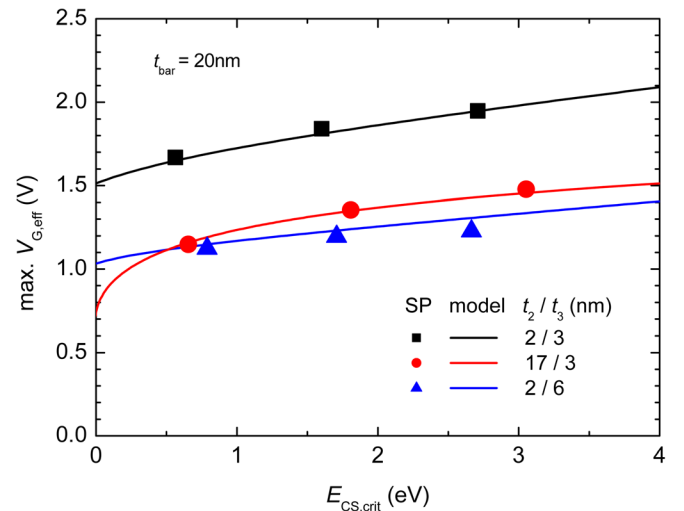


FIG. 8. (Color online) Maximum usable effective gate voltage as a function of the critical surface potential for three combinations of  $t_2$  and  $t_3$ . The variation of the critical surface potential is achieved by varying  $N_D$ . Analytical and Schrödinger-Poisson results are compared. In the analytical models the linear fit of  $\varphi_p(N_D)$ , see Fig. 7, is used.

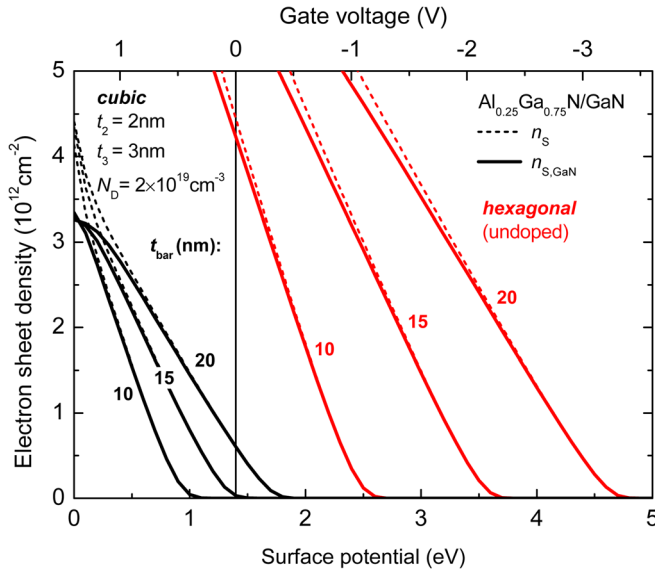


FIG. 9. (Color online)  $n_s(E_{CS})$  curves for cubic and hexagonal heterostructures with three different barrier thicknesses obtained from Schrödinger-Poisson simulations.

structure with  $t_2 = 17$  nm (where  $t_1 = 0$ ). In order to find an appropriate layer structure for a normally-off HEMT, one should bear in mind that because of the relation

$$V_{th} = (\Phi_B - E_{CS}^{th})/q, \quad (21)$$

$E_{CS}^{th}$  should be small in order to get a positive  $V_{th}$ . On the other hand, for proper transistor operation the applied  $E_{CS}$  must be positive (i.e.,  $V_G < \Phi_B/q$ ) to limit the gate current. Hence, to achieve large 2DEG densities, while limiting  $E_{CS}^{th}$ ,  $E_{CS}^{crit}$  should be close to zero. For the structure with  $t_2 = 2$  nm and  $t_3 = 3$  nm, this is the case for  $N_D \approx 2 \times 10^{19} \text{ cm}^{-3}$ , as can be seen from Fig. 7.

In case the threshold voltage is still negative, which mainly depends on the Schottky contact, the barrier thickness

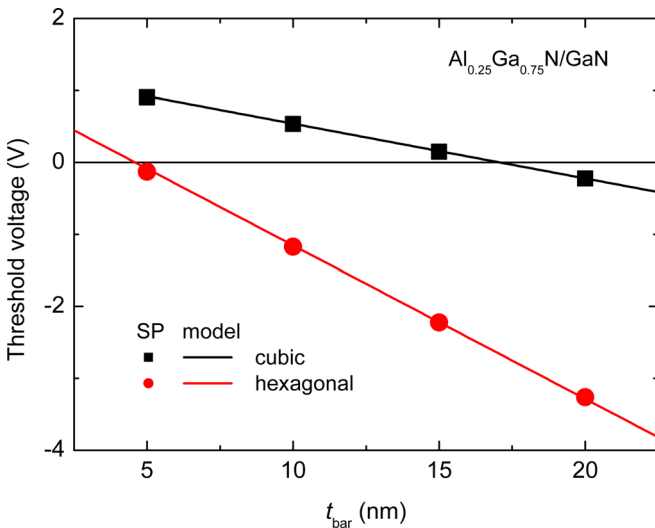


FIG. 10. (Color online) Threshold voltage as a function of the barrier thickness for cubic and hexagonal heterostructures. For the cubic heterostructure, the parameters of the doping layer ( $t_2, t_3, N_D$ ) are the same as in Fig. 9. Analytical and Schrödinger-Poisson results are shown.

may be reduced. This is illustrated in Fig. 9, where  $n_s(E_{CS})$  curves are shown for three different barrier thicknesses, while  $t_2$  and  $t_3$  are held constant. Also shown for comparison are the curves for hexagonal  $\text{Al}_{0.25}\text{Ga}_{0.75}\text{N}/\text{GaN}$  heterostructures with the same  $t_{bar}$ . The upper x axis again shows the gate voltage assuming a Schottky barrier height of 1.4 eV. As can be seen, for  $t_{bar} = 15$  nm the threshold voltage of the cubic heterostructure is positive, while for hexagonal material  $V_{th}$  remains negative even for a 10-nm thin AlGa barrier. According to Fig. 10, for the hexagonal heterostructure the barrier has to be made thinner than 5 nm to get a positive  $V_{th}$ . This clearly demonstrates the advantage of using cubic AlGaN/GaN for normally-off transistor applications instead of hexagonal material.

## V. CONCLUSION

Our study shows that cubic GaN-based HEMTs can be a promising alternative to their hexagonal counterparts, in particular for normally-off transistor applications. The absence of polarization effects in cubic AlGaN/GaN allows the designer to adjust the 2DEG density via the doping of the AlGa barrier without affecting the conduction band offset. Doping of the barrier, however, can lead to undesirable saturation effects of the 2DEG density. The analytical model developed in this work describes the critical gate voltage for the onset of saturation effects very well for a generic doped heterostructure that covers a wide range of realistic device designs. As a general guideline to maximize the usable effective gate voltage, the doped layer should be as close as possible to the heterojunction whereas the donor density should be large. While the thickness of the doped layer does not directly affect the maximum usable effective gate voltage, a narrow doping layer is beneficial for a positive threshold voltage. Our model can be helpful to find the optimum doping level for a normally-off HEMT design.

## ACKNOWLEDGMENTS

This work was supported by DFG under Contract Nos. SCHW 729/7-1, AS 107/4-1, and PE 624/7-1.

<sup>1</sup>U. K. Mishra, L. Shen, T. E. Kazior, and Y.-F. Wu, *Proc. IEEE* **96**, 287 (2008).

<sup>2</sup>J. Y. Duboz, *Phys. Status Solidi A* **176**, pp. 5 (1999).

<sup>3</sup>The International Technology Roadmap for Semiconductors, <http://public.itrs.net/>, 2011.

<sup>4</sup>B. S. Khalil, E. Bahat-Treidel, F. Schnieder, and J. Würfl, *IEEE Trans. Electron Devices* **56**, 361 (2009).

<sup>5</sup>S. Tirelli, D. Marti, H. Sun, A. R. Alt, H. Benedickter, E. L. Piner, and C. R. Bolognesi, *IEEE Electron Device Lett.* **34**, 296 (2010).

<sup>6</sup>O. I. Saadat, J. W. Chung, E. L. Piner, and T. Palacios, *IEEE Electron Device Lett.* **30**, 1254 (2009).

<sup>7</sup>M. Ishida, Y. Uemoto, T. Ueda, T. Tanaka, and D. Ueda, *Proc. IPEC*, 1014 (2010).

<sup>8</sup>M. Südow, M. Fagerlind, M. Thorsell, K. Andersson, N. Billström, P.-A. Nilsson, and N. Rosman, *IEEE Trans Microwave Theory Tech.* **56**, 1827 (2008).

<sup>9</sup>Y. F. Wu, B. P. Keller, S. Keller, D. Kapolnek, P. Kozodoy, S. P. Denbaars, and U. K. Mishra, *Appl. Phys. Lett.* **69**, 1438 (1996).

<sup>10</sup>J. Burm, W. J. Schaff, G. H. Martin, L. F. Eastman, H. Amano, and I. Aka-saki, *Solid-State Electron.* **41**, 247 (1997).

<sup>11</sup>R. Gaska, J. W. Yang, A. Osinsky, Q. Chen, M. Asif Khan, A. O. Orlov, G. L. Snider, and M. S. Shur, *Appl. Phys. Lett.* **72**, 707 (1998).

- <sup>12</sup>O. Ambacher, J. Smart, J. R. Shealy, N. G. Weimann, K. Chu, M. Murphy, R. Dimitrov, L. Wittmer, M. Stutzmann, W. Rieger, and J. Hilsenbeck, *J. Appl. Phys.* **85**, 3222 (1999).
- <sup>13</sup>E. Frayssinet, W. Knap, P. Lorenzini, N. Grandjean, J. Massies, C. Skierbiszewski, T. Suski, I. Grzegory, S. Porowski, G. Simin, X. Hu, M. Asif Khan, M. S. Shur, R. Gaska, and D. Maude, *Appl. Phys. Lett.* **77**, 2551 (2000).
- <sup>14</sup>V. Kumar, W. Lu, R. Schwindt, A. Kuliev, G. Simin, J. Yang, M. A. Khan, and I. Adesida, *IEEE Electron Device Lett.* **23**, 455 (2002).
- <sup>15</sup>T. Palacios, A. Chakraborty, S. Rajan, C. Poblenz, S. Keller, S. P. DenBaars, J. S. Speck, and U. K. Mishra, *IEEE Electron Device Lett.* **26**, 781 (2005).
- <sup>16</sup>T.-H. Yu and K. F. Brennan, *IEEE Trans. Electron Devices* **50**, 315 (2003).
- <sup>17</sup>T. Sadi, R. W. Kelsall, and N. J. Pilgrim, *IEEE Trans. Electron Devices* **53**, 2892 (2006).
- <sup>18</sup>O. Ambacher, J. Majewski, C. Miskys, A. Link, M. Hermann, M. Eickhoff, M. Stutzmann, F. Bernardini, V. Fiorentini, V. Tilak, B. Schaff, and L. F. Eastman, *J. Phys.: Condens. Matter* **14**, 3399 (2002).
- <sup>19</sup>A. Sozza, C. Dua1, E. Morvan, M. A. DiForte-Poisson, S. Delage, F. Rampazzo, A. Tazzoli, F. Danesin, G. Meneghesso, E. Zanoni, A. Curutchet, N. Malbert, N. Labat, B. Grimberty, and J.-C. De Jaeger, *Tech. Dig. IEDM*, 590 (2005).
- <sup>20</sup>J. Joh and J. A. del Alamo, *Tech. Dig. IEDM*, 1 (2006).
- <sup>21</sup>J. Joh, L. Xia, and J. A. del Alamo, *Tech. Dig. IEDM*, 385 (2007).
- <sup>22</sup>A. Chini, F. Fantini, V. Di Lecce, M. Esposito, A. Stocco, N. Ronchi, F. Zanon, G. Meneghesso, and E. Zanoni, *Tech. Dig. IEDM*, 169 (2009).
- <sup>23</sup>E. Tschumak, R. Granzner, J. K. N. Lindner, F. Schwierz, K. Lischka, H. Nagasawa, M. Abe, and D. J. As, *Appl. Phys. Lett.* **96**, 253501 (2010).
- <sup>24</sup>J. Kolník, İ. H. Oğuzman, K. F. Brennan, R. Wang, P. P. Ruden, and Y. Wang, *EJ. Appl. Phys.* **78**, 1033 (1999).
- <sup>25</sup>B. E. Foutz, L. F. Eastman, U. V. Bhapkar, and M. S. Shur, *Appl. Phys. Lett.* **70**, 2849 (1997).
- <sup>26</sup>F. Dessenne, D. Cichocka, P. Desplanques, and R. Fauquembergue, *Mater. Sci. Eng., B* **50**, 315 (1997).
- <sup>27</sup>M. Farahmand and K. F. Brennan, *IEEE Trans. Electron Devices* **46**, 1319 (1999).
- <sup>28</sup>R. Brazis and R. Raguotis, *Opt. Quantum Electron.* **38**, 339–347 (2006).
- <sup>29</sup>J. G. Kim, A. C. Frenkel, H. Liu, and R. M. Park, *Appl. Phys. Lett.* **65**, 91 (1994).
- <sup>30</sup>T. Kitamura, Y. Ishida, X. Q. Shen, H. Nakanishi, S. F. Chichibu, M. Shimizu, and H. Okumura, *Phys. Status Solidi B* **228**, 599 (2001).
- <sup>31</sup>M. Abe, H. Nagasawa, S. Potthast, J. Fernandez, J. Schörmann, D. J. As, and K. Lischka, *IEICE Trans. Electron. E* **89-C**, 1057 (2006).
- <sup>32</sup>V. M. Polyakov, F. Schwierz, I. Cimalla, M. Kittler, B. Lübbbers, and A. Schober, *J. Appl. Phys.* **106**, 023715 (2009).
- <sup>33</sup>J. Zou, H. Dong, A. Gopinath, and M. Shur, *IEEE Trans. Electron Devices* **39**, 250 (1992).
- <sup>34</sup>V. M. Polyakov and F. Schwierz, *J. Appl. Phys.* **98**, 023709 (2005).
- <sup>35</sup>P. Rinke, M. Winkelkemper, A. Qteish, D. Bimberg, J. Neugebauer, and M. Scheffler, *Phys. Rev. B* **77**, 075202 (2008).
- <sup>36</sup>N. F. Mott, *Philos. Mag.* **6**, 287 (1961).
- <sup>37</sup>D. Delagebeaudeuf and N. T. Linh, *IEEE Trans. Electron Devices* **29**, 955 (1982).
- <sup>38</sup>P. C. Chao, M. S. Shur, R. C. Tikerio, K. H. G. Duh, P. M. Smith, J. M. Ballingall, P. Ho, and A. A. Jabra, *IEEE Trans. Electron Devices* **36**, 461 (1989).
- <sup>39</sup>S. Luryi, *Appl. Phys. Lett.* **52**, 501 (1988).
- <sup>40</sup>D. L. John, L. C. Castro, and D. L. Pulfrey, *J. Appl. Phys.* **96**, 5180 (2004).
- <sup>41</sup>T. J. Drummond, H. Morkoc, K. Lee, and M. Shur, *IEEE Electron Device Lett.* **3**, 338 (1982).
- <sup>42</sup>F. Schwierz and J. J. Liou, *Modern Microwave Transistors* (J. Wiley & Sons, New York, 2003).